A Multiresolution Framework for Local Similarity based Image Denoising

Nasir Rajpoot[a,*], Irfan Butt[b]

[a]*Department of Computer Science, University of Warwick, Coventry CV4 7AL, UK*
[b]*Banque Saudi Fransi, Riyadh, Saudi Arabia*

Abstract

In this paper, we present a generic framework for denoising of images corrupted with additive white Gaussian noise based on the idea of regional similarity. The proposed framework employs a similarity function using the distance between pixels in a multidimensional feature space, whereby multiple feature maps describing various local regional characteristics can be utilized, giving higher weight to pixels having similar regional characteristics. An extension of the proposed framework into a multiresolution setting using wavelets and scale space is presented. It is shown that the resulting multiresolution multilateral (MRM) filtering algorithm not only eliminates the coarse-grain noise but can also faithfully reconstruct anisotropic features, particularly in the presence of high levels of noise.

Keywords:
Image Denoising, Bilateral Filtering, Local Image Statistics

1. Introduction

Denoising of an image refers to the removal of noise from the observed image and is often used as a pre-processing step before understanding and analysis of the image scene can take place. Various non-linear filtering methods have been proposed in the literature aimed at preserving edges during image denoising. Anisotropic diffusion [1], one of the most popular non-linear filtering methods, uses local conduction coefficients of the gradient magnitude function allowing it to preserve as well as sharpen the edges. However, it

*Corresponding author: nasir@dcs.warwick.ac.uk

is well known that the original Perona & Malik scheme tends to oversharpen edges, is a slowly converging non-linear iterative process, and may result in a piecewise smoothed version of the image [2]. While the oversharpening and slow convergence issues may have largely been overcome by works such as regularized and robust anisotropic diffusion [3, 4], anisotropic diffusion remains ill-suited for denoising of images containing textured patterns.

Shrinkage methods in the transform domain approximate the image by modeling and efficiently representing important image features such as discontinuities [5], edges [6, 7, 8], curves [9, 10, 11], contours [12, 13], ridges [14, 15], and textured regions [16, 17, 18, 19] present in the image or locally linear planes [20] in video sequences. Generally speaking, shrinkage methods first transform the image into some other domain, highlighting important image features, and thresholding the transform coefficients. Two major limitations of the shrinkage methods are that they exhibit (*a*) pseudo-Gibbs and (*b*) fake feature types of artifacts in images corrupted with medium to high levels of noise. The pseudo-Gibbs or *ringing* artifacts are generated due to there being insufficient number of coefficients for reconstruction of image features, while the *fake feature* artifacts such as those visible in contourlets [13] and wave atoms [19] result from the association of noisy image pixels with perceived image features.

The non-local means (NL-Means) algorithm proposed by Buades *et al.* [21] demonstrated that spatial filtering could benefit from searching for pixels of similar intensities in the whole image and averaging them. A major bottleneck of this type of approach, however, is the high computational complexity of a global search for pixels of similar intensity. Several fast adaptations of NL-Means have been proposed in the literature [22, 23, 24, 25]. Notwithstanding all the recent advances, the base NL-Means suffers from *fake texture* type of artifacts and is not as robust on high levels of noise, as shown in Section 4. In recent years, several hybrid domain methods have been proposed. These methods operate by altering both pixel intensity values and transform domain coefficients. The pointwise SA-DCT filtering [26] uses shape-adaptive discrete cosine transform (SA-DCT) in conjunction with the anisotropic local polynomial approximation (LPA) to remove noise from images. Block-matching and 3D filtering (BM3D) [27, 28] is another hybrid domain denoising method. It uses three main steps to denoise the image: 3D transformation of a group of *similar* blocks including a block centered around the current pixel, shrinkage of the transform spectrum, and inverse 3D transformation. Hybrid domain methods have demonstrated superior

performance over several other state-of-the-art methods.

Bilateral filtering [29] is another non-linear filtering method which can be regarded as an extended version of the lowpass Gaussian filtering. In essence, it is a simple combination of a domain filter, similar to the Gaussian filter, and a range filter which is a Gaussian function of local intensity differences. The main idea is that only perceptually analogous colors are averaged together to avoid unexpected color combination in images. Barash [30] unified anisotropic diffusion and non-linear bilateral filtering as another effective edge preserving filtering technique. However, one of the main limitations of bilateral filtering is that the range filter coefficients rely heavily on actual pixel intensity values, as it does not take into account any regional characteristics, which may in turn have been influenced by noise therefore potentially resulting in smoothed textured regions.

In order to overcome the limitations of bilateral filtering, Garnett *et al.* [31] proposed a trilateral filter employing a local image statistic for identifying the noisy pixels. The trilateral filter proposed in [31] was mainly aimed at denoising images corrupted with impulse noise, although it was shown to be effective for removing Gaussian and mixed noise too. The weighting function used by Garnett *et al.*'s trilateral filter contains spatial, radiometric, and impulsive components. A third weighting function, the impulsive component based on a rank-order statistic of absolute differences (ROAD), removes high frequency impulse noise. The resulting trilateral filter performs well in removing mixed noise as well as in removing impulse noise. Another trilateral filter was presented in [32] for high contrast images and meshes. Recently, a working paper by Yu *et al.* [33] proposed a third weighting function based on the energy of steerable filters [34] and applied an improved version of the bilateral filter, named by the authors as multilateral filtering, to denoising of runway images.

In this paper, we present a generic framework for denoising of images using local similarity of pixels. We propose an extension of non-linear bilateral filtering, also termed as *multilateral filtering*, for denoising of images that were corrupted with Gaussian white noise and consist of smooth regions, edge features, as well as textured areas. The proposed filtering operates simultaneously in three or more dimensions: *domain* filtering, *range* filtering, and K-dimensional *feature* filtering for $K \geq 1$. The first two dimensions are the same as those employed in bilateral filtering. In the larger dimensions, filtering is done based on the similarity of a pixel in the neighborhood to its center pixel. A set of local features is computed for each pixel using

its local neighborhood. Filtering based on features can proceed by either concatenating the features into a feature vector or by cascading the filters for each feature. In this work, we have chosen the former route for simplicity and efficiency reasons. This adaptive non-linear filtering results in feature (e.g., edge and texture) preserving images by giving larger weights to *similar* pixels and smaller weights to pixels that are different, thus similarities among pixels are not only defined by intensity of pixels but also by features associated with these pixels.

In the next section, we propose a local similarity based framework for image denoising. A comparison of various statistical and structural features, as discussed in Section 2, reveals that local energy is an effective measure of local similarity. We extend the proposed framework in a multiresolution setting in Section 3 and show in Section 4 that the multiresolution version of our algorithm is particularly effective for denoising images corrupted with high levels of noise.

2. The Proposed Framework

Since our method is a generalization of bilateral filtering, we provide here a brief description of bilateral filtering for the sake of completeness. Bilateral filters proposed by Tomasi & Manduchi [29] belong to a class of non-linear filters designed for edge preserving image denoising. They operate by convolving a given image with a combination of domain and range filters. The domain filter contains the Gaussian domain weights computed by the geometric closeness function $D(\mathbf{i},\mathbf{j})$, where $D(\mathbf{i},\mathbf{j})$ represents the Euclidean distance between the origin pixel at $\mathbf{i}$ and a nearby pixel at $\mathbf{j}$. The range filter, on the other hand, contains Gaussian range weights computed using an intensity difference function $R(\mathbf{i},\mathbf{j})$, where $R(\mathbf{i},\mathbf{j})$ gives the absolute difference between intensity values $I(\mathbf{i})$ and $I(\mathbf{j})$ corresponding to locations $\mathbf{i}$ and $\mathbf{j}$. The range filter is such that the larger the difference between two intensity values at $\mathbf{i}$ and $\mathbf{j}$, the smaller is the corresponding weight and vice versa. Let $G_{d,\mathbf{i}}$ and $G_{r,\mathbf{i}}$ respectively denote the domain and range filters, as defined below:

$$G_{d,\mathbf{i},\mathbf{j}} = \exp\left(-0.5[D(\mathbf{i},\mathbf{j})/\sigma_d]^2\right) / \sum_{\mathbf{j}\in N_\mathbf{i}} G_{d,\mathbf{i},\mathbf{j}}, \quad (1)$$

$$G_{r,\mathbf{i},\mathbf{j}} = \exp\left(-0.5[R(\mathbf{i},\mathbf{j})/\sigma_r]^2\right) / \sum_{\mathbf{j}\in N_\mathbf{i}} G_{r,\mathbf{i},\mathbf{j}}, \quad (2)$$

$\forall \mathbf{j} \in N_{\mathbf{i}}$, where $N_{\mathbf{i}}$ denotes the set of pixel coordinates in the local neighborhood of the center location $\mathbf{i}$, and σ_d and σ_r denote widths of the two Gaussian kernels. A bilateral filter is simply a product of the domain filter $G_{d,\mathbf{i}}$ and the range filter $G_{r,\mathbf{i}}$, where $G_{d,\mathbf{i}} = \{G_{d,\mathbf{i},\mathbf{j}},\ \forall \mathbf{j} \in N_{\mathbf{i}}\}$ and $G_{r,\mathbf{i}} = \{G_{r,\mathbf{i},\mathbf{j}},\ \forall \mathbf{j} \in N_{\mathbf{i}}\}$. A given image $\mathbf{I}$ is then convolved with the bilateral filter to obtain the denoised image $\hat{\mathbf{I}}$. For the pixel at location $\mathbf{i}$, $\hat{I}(\mathbf{i})$ is obatined as follows,

$$\hat{I}(\mathbf{i}) = (G_{d,\mathbf{i}} \cdot G_{r,\mathbf{i}}) \ * \ N_{\mathbf{i}} \tag{3}$$

$\forall \mathbf{i} \in \mathcal{C}$, where $\mathcal{C}$ denotes a set of all image coordinates and $N_{\mathbf{i}}$ denotes the neighborhood of pixel at location $\mathbf{i}$ as defined above.

As mentioned earlier in Section 1, one of the other major limitations of bilateral filtering is that the range filter coefficients rely heavily on actual pixel intensity values which may in turn have been influenced by noise. The range filter computed in this way may consider two noisy pixels to be similar when they happen to have similar intensity values only because of the influence of noise. It assumes that the similarity of two pixels can be determined just by analyzing their intensity values. Furthermore, bilateral filtering does not take into account any regional (e.g., textural) features, which can often be computed from analysis of the local statistical or structural properties. Several variations on the theme of bilateral filtering can be found in the literature. Multiresolution bilateral filtering (MRB) [35] is a local hybrid denoising method which employs both spatial domain bilateral filtering as well as wavelet shrinkage in order to remove coarse-grain (i.e., low frequency) noise from images. Yu *et al.* [36] recently proposed a denoising algorithm based on bilateral filtering on the result of denoising in the wavelet domain by modeling the wavelet coefficients using a trivariate Gaussian distribution. However, most of these methods also suffer from the limitations inherent to bilateral filtering.

In the next section, we present a generic framework for image denoising based on the weighted averaging of image pixels using the idea of *regional similarity* in order to overcome the above limitations.

2.1. The Proposed Framework

The overall concept of our method is illustrated in Fig. 1. First, we compute a set of suitable features for the input image $\mathbf{I}$. These features should characterize the regional similarities of a pixel's neighborhood such that two pixels belonging to the same region have a high similarity and vice

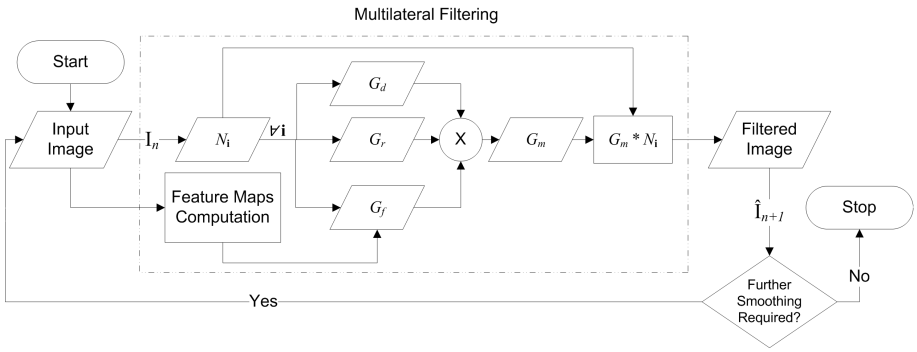

Figure 1: The Proposed Iterative Multilateral Filtering Framework

versa. By the same token, if two pixels belong to a similar kind of edge feature in the image, this should also be reflected by a relatively high value of the similarity function. Once a suitable set of features has been computed, the algorithm proceeds by computing the domain and range filters, as described in the previous section, as well as the *feature filter*. As stated earlier in Section 1, the computed features are concatenated in the form of a feature vector $\mathbf{f_i} = \{f_1(\mathbf{i}), f_2(\mathbf{i}), \ldots, f_K(\mathbf{i})\}$, where $f_k(\mathbf{i})$ denotes the kth feature for the pixel at $\mathbf{i}$ and K denotes the total number of features computed per pixel. The adaptive feature filter is then defined as follows,

$$G_{f,\mathbf{i},\mathbf{j}} = \exp\left(-||\mathbf{f_i} - \mathbf{f_j}||^2/2\sigma_f^2\right) / \sum_{\mathbf{j}\in N_\mathbf{i}} G_{f,\mathbf{i},\mathbf{j}}, \tag{4}$$

$\forall \mathbf{j} \in N_\mathbf{i}$, where $N_\mathbf{i}$ is as defined above and σ_f is width of the Gaussian kernel associated with the feature filter. Let $G_{f,\mathbf{i}} = \{G_{f,\mathbf{i},\mathbf{j}},\ \forall \mathbf{j} \in N_\mathbf{i}\}$. The filtered image $\hat{\mathbf{I}}$ can then be computed by taking a convolution of the input image $\mathbf{I}$ with the product $G_{m,\mathbf{i}}$ of the three Gaussian kernels as given below,

$$G_{m,\mathbf{i}} = (G_{d,\mathbf{i}} \cdot G_{r,\mathbf{i}} \cdot G_{f,\mathbf{i}}). \tag{5}$$

For a particular pixel at location $\mathbf{i}$, the denoised intensity value is computed as follows,

$$\hat{I}(\mathbf{i}) = G_{m,\mathbf{i}}\ *\ N_\mathbf{i}, \tag{6}$$

$\forall \mathbf{i} \in \mathcal{C}$. This completes one iteration of multilateral filtering.

2.2. Feature Normalization

It is worth noting that for different features put together in the form of a feature vector, all individual features $f_k(\mathbf{i})$, $\forall k = 1, 2, \ldots, K$ are normalized

to have a zero mean and a unit variance as follows,

$$f_k(\mathbf{i}) \longleftarrow \left(\frac{f_k(\mathbf{i}) - \mu_k}{\sigma_k} \right) \tag{7}$$

where μ_k and σ_k respectively denote mean and standard deviation of values of the kth feature for all pixels. Normalization of all features in this way ensures that equal weight is given to all and no single one is allowed to dominate.

Normalization of features in this way works well when the images are corrupted by Gaussian noise. But if the image is corrupted by a noise other than Gaussian, for example impulse noise, we may need to use some other linear transformation technique to normalize the features. This is because a linear transformation does not change the distribution of the data whereas the normalization in equation (7) has the potential of modifying the distribution of $f_k(\mathbf{i})$.

2.3. Iterative Multilateral Filtering

Although the original idea of bilateral filtering was non-iterative, Barash [30] showed that an iterative application of bilateral filtering may be required in images with high levels of noise. Using the robust median estimate [37] for noise standard deviation σ_n in the smoothed image, we can determine if further smoothing is required. If so, another iteration of multilateral filtering is performed on the result $\mathbf{I}_n$ of the previous iteration to obtain $\hat{\mathbf{I}}_{n+1}$. Needless to say, we start with $\mathbf{I}_0 = \mathbf{I}$.

Experiments with iterative bilateral and iterative multilateral filtering were conducted by increasing the number of iterations for a fixed level of noise. Results of these experiments on the *House* and *Monarch* images (cf. Fig. 5) for a total of ten iterations and two different noise levels $\sigma_n = 30$ (medium noise level) and $\sigma_n = 75$ (high noise level) are shown in Fig. 2. It can be observed in these results that near-optimal denoising results were obtained within 2–3 iterations for medium noise level ($\sigma_n = 30$) with not much improvement gained from any further iterations. For high level of noise ($\sigma_n = 75$), however, small but steady improvements continue to be made with increased number of iterations of both bilateral and multilateral filtering. It can also be seen from these plots that multilateral filtering is consistently outperforming bilateral filtering for both these images. Similar behavior was observed in other images as well. It can also be noted from Fig. 2 that the PSNR for *Monarch* at $\sigma_n = 30$ decreases after 2 iterations.

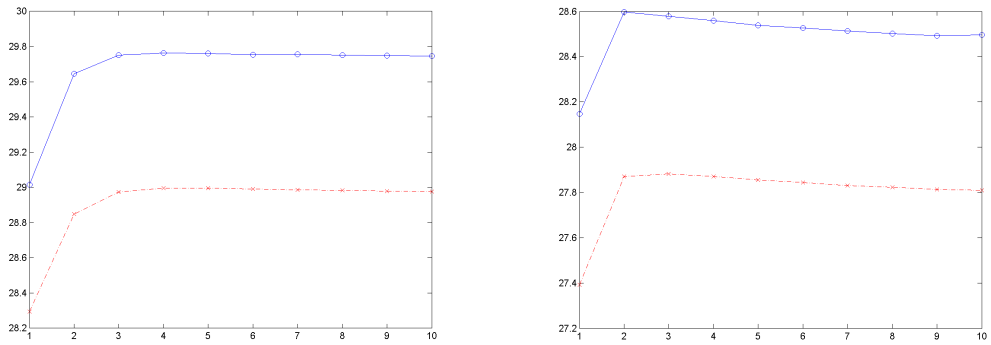

(*a*) *House* ($\sigma_n = 30$) (*b*) *Monarch* ($\sigma_n = 30$)

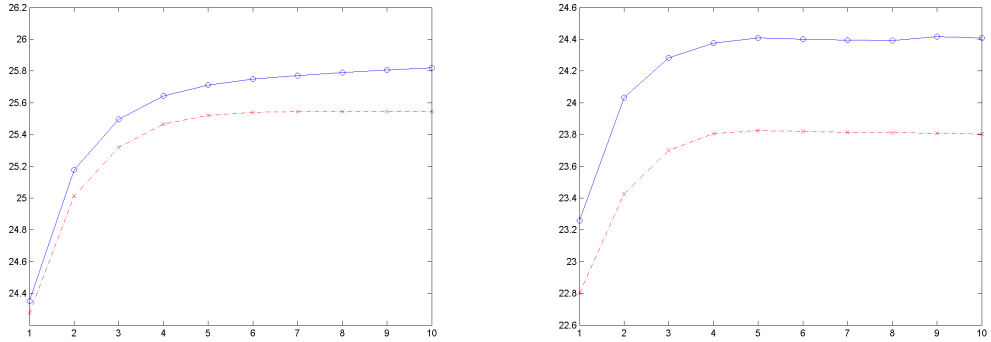

(*c*) *House* ($\sigma_n = 75$) (*d*) *Monarch* ($\sigma_n = 75$)

Figure 2: Plots of PSNR (dB) against number of iterations for bilateral (dashed line with red $\times$'s) and multiatleral filtering (solid line with blue o's) for *House* and *Monarch* using (a,b) $\sigma_n = 30$ and (c,d) $\sigma_n = 75$.

We believe this behavior may be due to the piecewise smooth nature of this particular image. For a fair comparison with other published algorithms though, in the remainder of this paper we run our method with one iteration only.

2.4. Experiments using Local Statistical and Structural Features

We conducted a large number of experiments with both synthetic and real-world images corrupted with additive Gaussian white noise (AWGN). Two aspects of the proposed framework were subject of our investigation. First, which type of features are useful in describing regional similarity for

denoising purposes. Second, how the proposed method fares as compared to the original bilateral filtering (`BF`) and other state-of-the-art methods.

To answer the first question, we conducted experiments with a number of local statistical features such as local energy (`E`) defined as the sum of square of pixel intensity values in a local neighborhood $N_{\mathbf{i}}$ for some arbitrary pixel location $\mathbf{i}$, local variance (`V`) defined over $N_{\mathbf{i}}$, local median (`M`) defined as the median of pixel intensity values in $N_{\mathbf{i}}$, local entropy defined over pixel intensity values in $N_{\mathbf{i}}$ and two combinations of these features namely energy and median (`M,E`), and energy and variance (`V,E`). Experiments were also conducted using two local structural features: multiscale wavelet edge maps (`Edge`) [38] and pyramidal histograms of orientation gradients (`Phog`) features [39].

Experimental results for four 256-level greyscale images, each of a 512×512 resolution and shown in Fig. 5, are given in Table 1. Two of these images contain textural patterns: *Cosine Grating*, a synthetic image containing two cosine waves, and a *Fingerprint* image. The other two images are taken from the standard real-world test image databases: *Lena* image consisting of relatively smooth regions and *Barbara* containing fine periodic textures at different orientations. Denoising performance is measured in terms of the Peak Signal to Noise Ratio (PSNR). For each greyscale test image, five noisy versions were created by adding white Gaussian noise with standard deviations 10, 20, 30, 40, and 100. The parameters of bilateral filtering were set as follows: the window size is 11×11, $\sigma_d = 1.8$, whereas σ_r is calculated in a way that PSNR computed from output image and original image is maximized. For our proposed method, we set the same parameter values for σ_d, σ_r for bilateral filtering as suggested in [29] to give a fair comparison. The value of σ_f is adjusted to maximize the PSNR. It can be seen from Table 1 that while the proposed multilateral filtering with a combination of local energy and variance achieves a PSNR gain of up to 6.22dB over the best bilateral filtering result in case of the *Cosine Grating* image at $\sigma_n = 20$, local energy `E` is the overall winner. This is due to the fact that measures of local variation, such as local entropy or local variance, are more sensitive to noise than local energy which has a low-pass effect. A more detailed analysis of local energy is given in the next section.

In order to address the second question posed at the start of this section, a detailed comparative evaluation of multilateral filtering with local energy (`Multilateral E`) is provided in Section 4, Tables 2 and 3. It is worth noting that in Table 1 that multilateral filtering behaves at least as well as a

Input Image	σ_n	BF [29]	Multilateral Filtering						
			Edge	Phog	V	E	M	M, E	V, E
Cosine Grating	10	30.23	31.58	30.57	33.50	33.10	31.70	33.05	**33.70**
	20	23.61	26.65	24.23	25.53	29.45	26.91	28.78	**29.83**
	30	21.81	24.42	23.00	23.60	**26.79**	24.34	25.82	26.54
	40	20.61	22.86	22.20	22.00	24.46	22.74	23.85	**24.55**
	100	17.80	18.93	18.80	18.10	**19.20**	18.8	19.05	19.00
Finger Print	10	32.12	32.12	32.12	32.68	**33.10**	32.30	32.77	32.93
	20	28.14	28.26	28.22	28.14	**29.61**	28.76	29.03	29.10
	30	24.73	25.00	25.00	24.73	**26.79**	26.34	26.59	26.10
	40	22.81	23.18	23.19	22.81	**24.97**	24.68	24.90	24.30
	100	19.29	19.29	19.35	19.29	**19.64**	19.60	19.62	19.47
Lena	10	33.75	33.75	33.75	34.00	**34.34**	34.05	34.22	34.10
	20	30.57	30.57	30.57	30.57	**31.13**	31.00	31.10	30.72
	30	28.82	28.82	28.82	28.82	**29.32**	29.27	29.31	28.90
	40	27.64	27.64	27.64	27.64	**28.03**	28.01	28.02	27.70
	100	22.88	22.88	22.88	22.88	22.88	22.88	22.88	22.88
Barbara	10	31.45	31.45	31.45	31.56	**31.71**	31.62	31.70	31.64
	20	27.19	27.19	27.19	27.19	**27.52**	27.41	27.50	27.33
	30	25.12	25.12	25.12	25.12	**25.36**	25.31	25.34	25.18
	40	23.98	23.98	23.98	23.98	**24.10**	24.06	24.09	23.98
	100	20.87	20.87	20.87	20.87	20.87	20.87	20.87	20.87
Average	-	25.67	26.23	25.95	26.15	**27.12**	26.53	26.92	26.94

Table 1: Results of Multilateral Filtering using Local Statistical and Structural Features in terms of PSNR (dB)

bilateral filter when the noise level is high, e.g., when $\sigma_n = 100$ for *Lena* and *Barbara*. In the presence of heavy noise, local statistical features may not provide much extra information about the regional characteristics of a pixel. However, better estimates of regional similarity can be obtained at lower resolutions and hence better denoising results can be achieved by extending the proposed framework to multiple resolutions, as shown in Section 3.

2.5. Best of the Local Features

As noted above, multilateral filtering with local energy almost always produces the best results as compared to other local features described in the previous section. In this section, we establish a relationship between local energy based similarity function and another regional similarity function used

by Non-Local Means (NL-Means) [21], a popular denoising algorithm. Let D_{nlm} denote the dissimilarity function used by NL-Means and $D_{\mathtt{E}}$ denote the dissimilarity function used by multilateral filtering with local energy. Both these functions are exponentiated with a negative sign and appropriate scaling factors (involving kernel bandwidths) in order to compute the values of a similarity function, which in turn affects the weights associated with the pixel values being averaged. The two dissimilarity functions can be expressed as follows,

$$D_{nlm}(\mathbf{i},\mathbf{j}) = \sum_{\mathbf{k}\in N_{\mathbf{i}},\mathbf{l}\in N_{\mathbf{j}}} (x_{\mathbf{k}} - x_{\mathbf{l}})^2 \tag{8}$$

and

$$D_{\mathtt{E}}(\mathbf{i},\mathbf{j}) = \sum_{\mathbf{k}\in N_{\mathbf{i}}} x_{\mathbf{k}}^2 - \sum_{\mathbf{l}\in N_{\mathbf{j}}} x_{\mathbf{l}}^2 \tag{9}$$

where $N_{\mathbf{i}}$ and $N_{\mathbf{j}}$ denote the neighborhoods of pixels at locations $\mathbf{i}$ and $\mathbf{j}$, respectively. Both $N_{\mathbf{i}}$ and $N_{\mathbf{j}}$ are of the same size and follow the same scan order. For the sake of argument, let us assume that $N_{\mathbf{i}}$ and $N_{\mathbf{j}}$ are the same for both D_{nlm} and $D_{\mathtt{E}}$. In other words, we assume that NL-Means is applied only locally[1]. It can be shown that $D_{\mathtt{E}}$ can be written in terms of D_{nlm} as follows,

$$D_{\mathtt{E}} = D_{nlm} + 2 \sum_{\mathbf{k}\in N_{\mathbf{i}},\mathbf{l}\in N_{\mathbf{j}}} x_{\mathbf{l}} |x_{\mathbf{k}} - x_{\mathbf{l}}|. \tag{10}$$

For the sake of simplicity, we have dropped the arguments $\mathbf{i},\mathbf{j}$ from both the dissimilarity functions. From the above equation, $D_{\mathtt{E}}$ can be expressed as a linear combination of D_{nlm} and sum of intensity differences between corresponding neighboring pixels in $N_{\mathbf{i}}$ and $N_{\mathbf{j}}$ weighted by the values of pixels in $N_{\mathbf{j}}$. In other words, $D_{\mathtt{E}}$ is sum of the l_2-norm based D_{nlm} and a scaled version of the l_1-norm of pointwise intensity differences for $N_{\mathbf{i}}$ and $N_{\mathbf{j}}$. This allows $D_{\mathtt{E}}$ to be more robust than the simple l_2-norm based D_{nlm} particularly in situations with high levels of noise, as illustrated later in Section 4, Table 3.

In order to illustrate the robustness of local energy based regional similarity in the presence of high levels of noise, we take 512×512 *Monarch*

[1]Without loss of generality, we make this assumption only to establish a relationship between D_{nlm} and $D_{\mathtt{E}}$. In fact, an extension of our algorithm is also possible in a non-local framework although such an extension has not been investigated in this work.

image corrupted with AWGN and $\sigma_n = 100$ as an example. Fig. 3 shows the comparative visual results of a 16×16 section of the *Monarch* image containing one of the wing lines, the feature map of noisy image using local energy by our proposed method works better than all the other techniques. It can be observed that both `MF-E` and `MRM-Wav` (cf. Section 3) have sharper edges as compared to Fig. 3(d)–(f) where Gaussian filtering, bilateral filtering, and NL-Means were used for denoising. Notice also the profile of feature filter function G_f computed on the center pixel of the wing line. Despite the presence of heavy noise (see Fig. $3(c)$), the feature filter G_f shown in Fig. $3(l)$ corresponds well to the line feature as compared to the intensity-based range filter G_r shown in Fig. $3(k)$.

2.6. Choice of Parameters

The result of denoising an image using bilateral filtering may vary significantly with the change in input parameters that make up the kernel bandwidths for spatial distance and photometric similarity. Typical approach to get the best set of parameters is to use a trial and error method until the best denoising result is obtained. Clearly, this can be a laborious and time consuming task. To the best of our knowledge, there is no widely accepted solution for the selection of optimal σ_d and σ_r with firm theoretical backing. Zhang & Gunturk [35] established an empirical relationship between σ_d ,σ_r and the noise standard deviation σ_n in case of bilateral filtering. The authors conducted extensive experimentation to minimize the Mean Squared Error (MSE) between original signal and noisy signal by varying the parameters σ_d, σ_r and σ_n. They showed that σ_d is relatively independent of the noise standard deviation σ_n and that the ideal value for σ_d was empirically found to be in the $[1.5, 2.1]$ interval while σ_n can be estimated using robust median estimator [37]. But in case of σ_r, the best value of σ_r is linearly related to the noise standard deviation σ_n if σ_d is kept constant. Linearity among optimal value of σ_r and σ_n still holds as σ_d is varied, resulting only in a change in slope with an increase in slope as σ_d becomes higher.

In this work, we have followed the recommendations of Zhang & Gunturk [35] for selecting σ_d and σ_r whereas the PSNR is calculated by comparing the denoised image with the original image. As for σ_f, it is adjusted so as to maximize the PSNR of the denoised image by running a sweep through the interval $[0.1, 1.0]$ with a step of 0.1. For calculation of the PSNR, Stein's unbiased risk estimate (SURE) based estimator for Mean Squared Error (MSE)

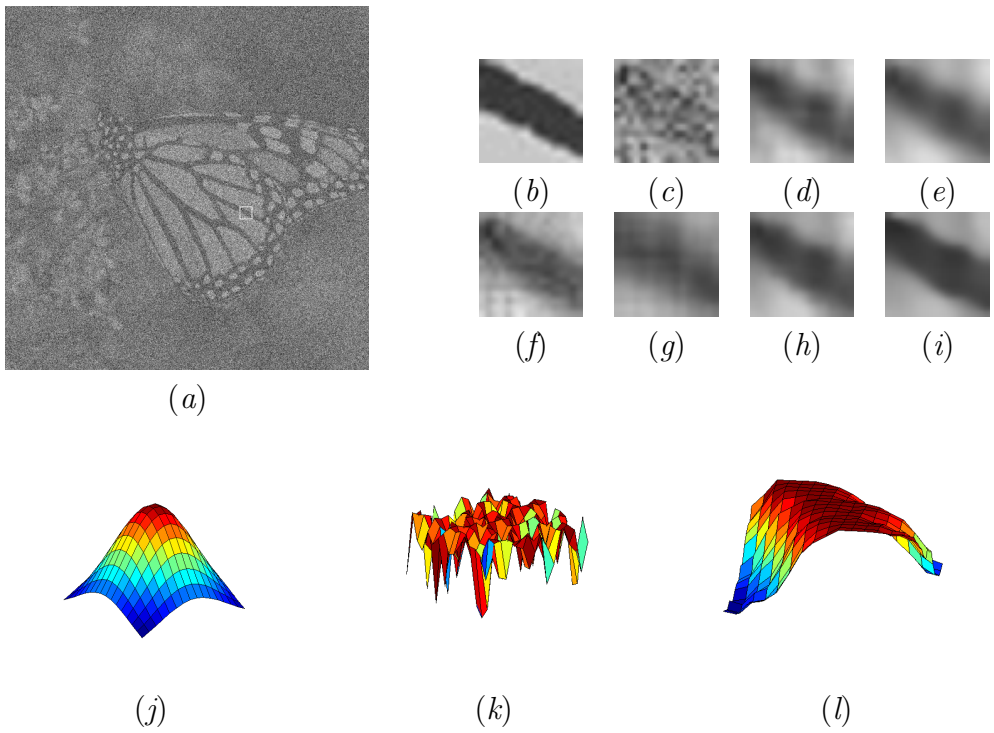

Figure 3: Illustration of the Idea of Local Energy based Filtering
(*a*) The 512×512 *Monarch* image corrupted with AWGN, $\sigma_n = 100$; (*b*)–(*i*) show a 16×16 section of the image containing one of the wing lines in the following order: (*b*) Original, (*c*) Noisy, (*d*) Denoised with a 5×5 Gaussian kernel, (*e*) Bilateral filtering result, (*f*) NL-Means filtering [21] result, (*g*) Local energy map using an 11×11 window, (*h*) Result of Multilateral Filtering with `E`, (*i*) Result of `MRM-Wav` (Section 3); (*j*)–(*l*) Filtering kernels in the order G_d, G_r, and G_f.

proposed recently by van de Ville & Kocher [25] for the non-local means algorithm may be extended for our method too.

3. Multiresolution Multilateral (MRM) Filtering

Noise in an image does not necessarily manifest itself as high frequency values. It may be present in low frequency regions too making it difficult to differentiate between genuine pixel values and low-frequency or coarse-grain noise. In this scenario, simple bilateral or multilateral filtering may not be hugely effective. One of the most recently proposed solutions is to use a

multiresolution framework [35], which performs filtering on low frequency wavelet subbands at different resolutions. The coarse-grain noise can be easily removed at higher scales. Multiresolution bilateral (MRB) Filtering [35] is an extension of bilateral filtering in which a bilateral filter is applied to the approximation (low-frequency) subbands and BayesShrink [37] is applied to high frequency subbands of the wavelet decomposition. One limitation of the MRB filtering method though is that, just as in case of bilateral filtering [29], the range filter coefficients rely heavily on actual pixel intensity values which may in turn have been influenced by noise. The range filter coefficients computed in this way may consider two noisy pixels to be similar when they happen to have similar intensity values due to the influence of noise, and so MRB filtering does not take into account local statistical or structural characteristics of the two noisy pixels. The other notable problem that MRB faces is the occurence of pseudo-Gibbs phenomena in the vicinity of discontinuities due to its employing a wavelet decomposition and BayesShrink [37] to denoise the high frequency bands.

In this section, we propose multiresolution multilateral (MRM) filtering which aims to overcome the limitations of both bilateral and MRB filtering. We show that MRM filtering is an effective filtering method for denoising images with textured patterns as well as faithfully reconstructing discontinuities such as edges and curvilinear features in images. Two variants of MRM filtering are proposed: MRM in the wavelet domain and MRM in the scale space. In the remainder of this paper, we present the algorithmic details of these two variants of MRM filtering and present experimental results to demonstrate their effectiveness for denoising images.

3.1. MRM in the Wavelet Domain

In this section, we extend the proposed method of multilateral filtering described in Section 2 in a multiresolution framework, termed as `MRM-Wav`. This extension bears similarity to that of bilateral filtering in MRB [35]. However, one major difference is that our proposed method employs *feature filter* alongwith *domain* and *range filters* on multiple scales to denoise the image. Let $\mathcal{W}_n(\mathbf{I}) = \{HL^1, LH^1, HH^1, \ldots, HL^n, LH^n, HH^n, LL^n\}$, where $\mathbf{I}$ denotes the input image and HL^j, LH^j, HH^j, LL^j respectively denote the j-level horizontal detail, vertical detail, diagnoal detail, and lowpass subbands. The values of σ_r and σ_f are scaled by a factor of $(\sqrt{2})^j$ taking into account the increased dynamic range of the jth level wavelet subbands, whereas the

value of σ_d remains the same for all levels of the wavelet decomposition. The algorithmic details of `MRM-Wav` are given in Algorithm 1.

Algorithm 1 Multiresolution Multilateral Filtering in the Wavelet Domain (`MRM-Wav`)

procedure MRMFILTERINGWAVELETDOMAIN($\mathbf{I}, n$)
  $\{HL^1, LH^1, HH^1, \ldots, HL^n, LH^n, HH^n, LL^n\} \leftarrow \mathcal{W}_n(\mathbf{I})$ ▷ Compute n-level wavelet transform
  for $j \leftarrow n, n-1 \ldots, 1$ **do**
    $\widehat{HL}^j \leftarrow \mathcal{BS}(HL^j)$ ▷ Apply BayesShrink [37] on the jth level high frequency subbands
    $\widehat{LH}^j \leftarrow \mathcal{BS}(LH^j)$
    $\widehat{HH}^j \leftarrow \mathcal{BS}(HH^j)$
    if $j = 1$ **then**,
      $\widehat{LL}^j \leftarrow \mathcal{MF}(LL^j)$ ▷ Apply multilateral filtering on LL^1
      $\hat{\mathbf{I}} \leftarrow \mathcal{W}_1^{-1}(\widehat{HL}^j, \widehat{LH}^j, \widehat{HH}^j, \widehat{LL}^j)$ ▷ Reconstruct the preliminary denoised image
    else
      $\widehat{LL}^{j-1} \leftarrow \mathcal{W}_1^{-1}(\widehat{HL}^j, \widehat{LH}^j, \widehat{HH}^j, \widehat{LL}^j)$ ▷ Take 1-level inverse wavelet transform
    end if
  end for
  $\hat{\mathbf{I}} \leftarrow \mathcal{MF}(\hat{\mathbf{I}})$ ▷ Apply multilateral filtering again on $\hat{\mathbf{I}}$
  return $\hat{\mathbf{I}}$
end procedure

3.2. MRM in Scale Space

This variant of MRM filtering, termed as `MRM-Lap`, first decomposes the given image into a Laplacian pyramid [40]. A Laplacian scale space is used due to its shift invariance in order to avoid the Gibbs type of artifacts. Adaptive multilateral filtering is used to denoise the low frequency or Gaussian approximation subband and translation invariant packets (TIWP) [41] is applied on the high frequency subbands. TIWP is a very effective denoising technique on high frequency subbands because it further explores the high frequency subbands up to the maximum depth. Let $\mathcal{L}_n$ denote the forward

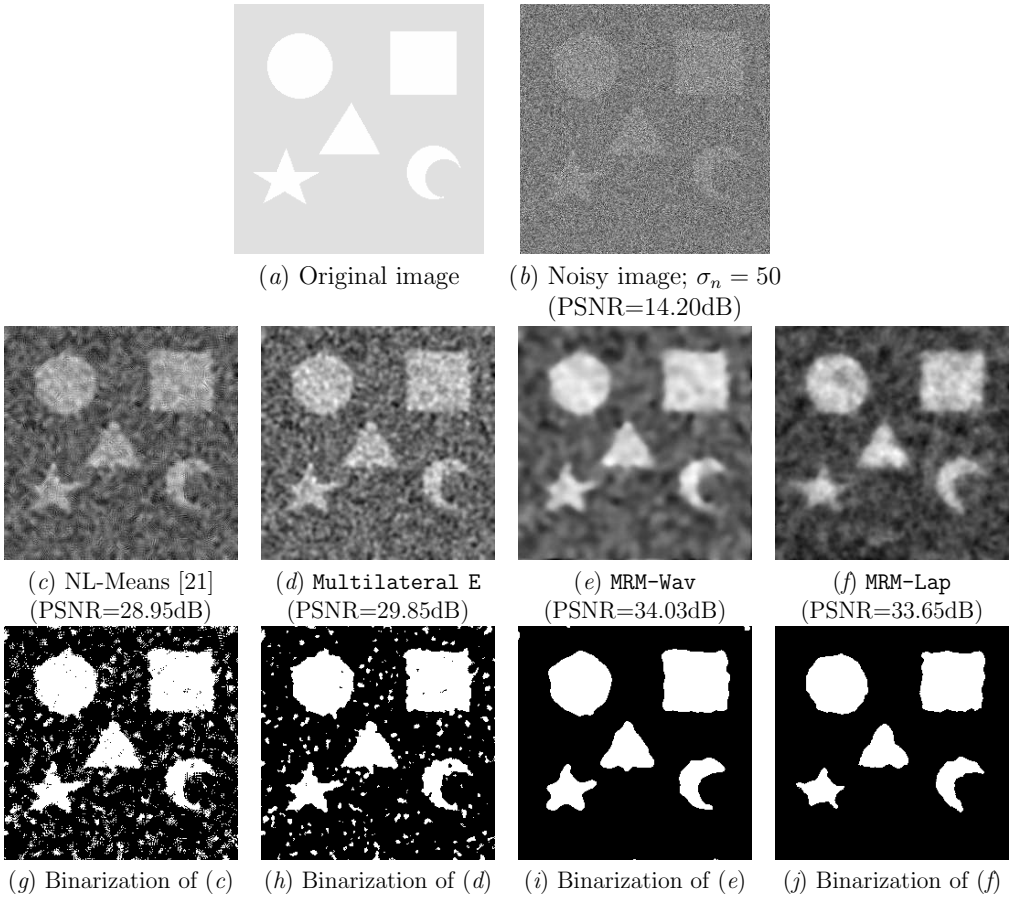

(*a*) Original image (*b*) Noisy image; $\sigma_n = 50$ (PSNR=14.20dB)

(*c*) NL-Means [21] (PSNR=28.95dB) (*d*) `Multilateral E` (PSNR=29.85dB) (*e*) `MRM-Wav` (PSNR=34.03dB) (*f*) `MRM-Lap` (PSNR=33.65dB)

(*g*) Binarization of (*c*) (*h*) Binarization of (*d*) (*i*) Binarization of (*e*) (*j*) Binarization of (*f*)

Figure 4: Results of Denoising and Binarization using Otsu's thresholds for 256×256 *Shapes*

n-level Laplacian pyramid operator given by, $\mathcal{L}_n(\mathbf{I}) = \{H_1, H_2, \ldots, H_n, L_n\}$, where $\mathbf{I}$ denotes the input image, H_j, $j = 1, \ldots, n$, denote the high frequency Laplacian subband and L_n denotes the lowest resolution and lowest frequency Gaussian approximation subband. The values of σ_d, σ_r, and σ_f remain unaltered for different levels of the Laplacian pyramid. The algorithmic details of `MRM-Lap` are given in Algorithm 2.

3.3. The Effectiveness of MRM

The effectiveness of MRM filtering is illustrated in Fig. 4 where denoising experiments were performed by adding white Gaussian noise of standard deviation 50 in *Shapes*, a simple image containing various smooth regions

Algorithm 2 Multiresolution Multilateral Filtering in the Scale Space (`MRM-Lap`)

procedure MRMFILTERINGSCALESPACE($\mathbf{I}, n$)
  $\{H_1, H_2, \ldots, H_n, L_n\} \leftarrow \mathcal{L}_n(\mathbf{I})$ ▷ Compute n-level Laplacian pyramid
  for $j \leftarrow 1, 2, \ldots, n$ **do**
    $\hat{H}_j \leftarrow \mathcal{TIWP}(H_j)$ ▷ Denoise H_j using TIWP shrinkage [41]
    $H_j \leftarrow \hat{H}_j$
  end for
  $\hat{\mathbf{I}} \leftarrow \mathcal{L}_n^{-1}(H_1, H_2, \ldots, H_n, L_n)$ ▷ Compute inverse Laplacian pyramid
  $\{H_1, L_1\} \leftarrow \mathcal{L}_1(\hat{\mathbf{I}})$ ▷ Compute 1-level Laplacian pyramid
  $\hat{L}_1 \leftarrow \mathcal{MF}(L_1)$ ▷ Apply multilateral filtering on L_1
  $\hat{\mathbf{I}} \leftarrow \mathcal{L}_1^{-1}(H_1, L_1)$ ▷ Compute 1-level inverse Laplacian pyramid
  $\hat{\mathbf{I}} \leftarrow \mathcal{MF}(\hat{\mathbf{I}})$ ▷ Apply multilateral filtering again on $\hat{\mathbf{I}}$
  return $\hat{\mathbf{I}}$
end procedure

consisting of geometric shapes against a flat background. Visual results of denoising with NL-Means [21], `Multilateral E`, `MRM-Wav`, and `MRM-Lap` (Section 3.2) can be seen in Fig. 4(c)–(f). Binarized versions of the denoising results using a simple thresholding operation are shown in Fig. 4(g)–(j). Thresholds were automatically selected using Otsu's method [42]. It can be observed from these binarized results that both `MRM-Wav` and `MRM-Lap` produce arguably better results for detection of the shapes' regions as compared to NL-Means. Such a method can be used for detection of objects against the background in a highly noisy environment.

4. Experimental Results

Comparative denoising results for various local statistical and structural features using single-resolution multilateral filtering were presented in Section 2.4, where we noted that local energy yielded the best denoising results on the whole. In this section, we pick local energy for computation of feature maps and present comparative results for single-resolution multilateral filtering and two versions of MRM filtering, the multiresolution version of our multilateral filtering algorithm, presented above. Although results for iterative multilateral filtering in Section 2.3 showed that better denoising results could be achieved using multiple iterations, we use only one iteration here to

give a fair comparison with other published methods.

Denoising experiments were conducted on seven of the eight 256-level greyscale images shown in Fig. 5. Five of these images are taken from the standard real-world test image databases: *Lena*, *House* and *Peppers* images have relatively smooth regions, while *Barbara* contains fine periodic textures at different orientations and *Fingerprint* consists mostly of coarse level anisotropic oscillatory patterns. Two other images were used in the testbed: *Monarch* image containing spotty patterns and coarse strongly oriented features (the wing lines), *Zebra* image containing periodic textures of coarse level anisotropic oscillatory features and smooth regions. The last four images were chosen to investigate the comparative performance of our algorithms on images containing approximately periodic textures and strongly oriented features or patterns, particularly in the presence of high levels of noise. Although `Multilateral E` was shown to achieve significant PSNR gains for the *Grating* image in Section 2, that image is omitted from these experiments due to its purely synthetic and somewhat artificial nature. Three levels of wavelet transform (for `MRM-Wav`) and Laplacian pyramid (`MRM-Lap`) were computed, as one risks blurring the lowpass band and introducing ringing artifacts if a higher number of levels of the transforms is used. For comparison of objective quality, denoising results in terms of the PSNR are presented for three methods presented in this paper, namely `Multilateral E` or `MF-E` (Section 2), `MRM-Wav`, and `MRM-Lap` (Section 3) in comparison to six other published methods: (1) the original bilateral filtering (`BF`) [29], (2) one of its recent variants known as saliency bilateral filtering (`SBF`) [43], two of the recently proposed transform-domain shrinkage methods in (3) `Contourlet MD` or `C-MD` [13] in the multi-scale contourlet domain with sharp localization in frequency and (4) wave atoms (`WA`) by Demanet & Ying [19] which aim to achieve good localization in space and frequency using Villemoes' wavelet packets [44] in the frequency domain, (5) a multiresolution version of bilateral filtering (`MRB`) [35], and (6) the standard non-local means filtering (`NL-Means` or `NLM`) [21] algorithm.

Two sets of experiments were conducted on the test images varying the level of Gaussian white noise from low–medium range ($\sigma_n = 10, 20, 30$) to high levels of noise ($\sigma_n = 50, 75, 100$). It is worth noting that a large body of denoising literature is concentrated in the low–medium range of noise level.

Input Image	σ_n	BF [29]	C-MD [37]	SBF [13]	WA [19]	NLM [21]	MF-E [Sec. 2]	MRB [35]	MRM-Wav [Sec. 3]	MRM-Lap [Sec. 3]
Finger-print	10	32.12	29.37	27.34	31.05	31.95	33.10	**33.51**	**33.51**	32.90
	20	28.14	26.44	23.45	27.06	29.11	**29.61**	28.98	29.07	27.95
	30	24.73	24.73	21.50	25.00	26.75	26.79	26.42	**26.82**	24.90
	Ave.	28.33	26.85	24.10	27.70	29.27	**29.83**	29.64	29.80	28.58
Lena	10	33.75	32.59	27.56	34.14	**35.16**	34.34	33.98	34.10	33.86
	20	30.57	31.20	23.45	30.78	**31.92**	31.13	31.31	31.56	30.54
	30	28.82	29.70	22.32	28.83	29.75	29.32	29.75	**30.01**	29.12
	Ave.	31.05	31.16	24.44	31.25	**32.28**	31.60	31.68	31.89	31.17
Barbara	10	31.45	30.16	27.67	33.25	**33.31**	31.71	31.61	31.65	32.28
	20	27.19	27.02	23.20	29.69	**29.89**	27.52	27.83	27.95	28.34
	30	25.12	25.30	21.64	**27.71**	27.45	25.36	25.55	25.63	26.58
	Ave.	27.92	27.49	24.17	30.22	**30.22**	28.20	28.33	28.41	29.07
House	10	33.81	32.19	27.54	34.05	**35.33**	34.45	33.54	33.65	34.47
	20	30.37	29.57	23.45	30.34	**32.17**	31.11	31.26	31.41	30.41
	30	28.35	28.00	22.33	28.21	**29.77**	29.08	29.18	29.75	29.21
	Ave.	30.84	29.92	24.44	30.87	**32.42**	31.55	31.33	31.60	31.36
Peppers	10	33.03	30.52	27.65	31.90	33.41	**33.61**	33.00	33.10	32.55
	20	29.34	28.12	23.34	28.37	**30.51**	30.00	29.80	29.95	29.00
	30	26.90	26.43	22.07	26.30	**28.29**	27.70	27.56	27.72	27.00
	Ave.	29.76	28.36	24.35	28.86	**30.74**	30.44	30.12	30.26	29.52
Monarch	10	32.82	31.25	27.55	32.00	32.8	**33.27**	32.32	32.32	32.48
	20	29.65	29.03	23.34	28.82	**30.53**	30.20	29.66	29.66	28.21
	30	27.38	27.52	22.02	27.00	**28.66**	28.15	28.20	28.30	26.31
	Ave.	29.95	29.27	24.30	29.27	**30.66**	30.54	30.06	30.09	29.00
Zebra	10	32.40	30.60	27.61	32.10	32.88	32.90	32.50	32.50	**33.00**
	20	28.45	27.70	23.27	28.60	**30.13**	29.15	28.70	28.70	28.53
	30	25.60	25.90	21.80	26.00	**27.80**	26.55	26.58	26.68	26.22
	Ave.	28.82	28.07	24.23	28.90	**30.27**	29.53	29.26	29.29	29.25
Average	-	29.52	28.73	24.29	29.58	**30.84**	30.24	30.06	30.19	29.71

Table 2: Comparative Image Denoising Results in terms of PSNR (dB) for Low–Medium Noise Levels

4.1. Experiments with Low–Medium Noise Levels

In Table 2, a comparison of denoising results for the test images corrupted with low–medium noise levels ($\sigma_n = 10, 20, 30$) is presented. It can be seen from this Table that although `NL-Means` is on average 0.6dB better than `MF-E` with `MRM-Wav` close behind, there are a few instances (*Peppers*, *Monarch*, and *Zebra*) where either of the two proposed methods yields the best PSNR value at $\sigma_n = 10$. It is also worth noting that the proposed methods compare favorably with all the other six published methods for *Fingerprint* at all three noise levels, on the whole nearly 3dB better than `Contourlet MD`, nearly 2.1dB better than wave atoms, and nearly 0.6dB better than `NL-Means`. This behavior for *Fingerprint* continues at $\sigma_n = 50$, as shown in the next section, until we get to relatively high noise levels

Input Image	σ_n	Median	BF [29]	C-MD [37]	SBF [13]	WA [19]	NLM [21]	MF-E [Sec. 2]	MRB [35]	MRM-Wav [Sec. 3]	MRM-Lap [Sec. 3]
Finger-print	50	21.04	21.61	22.80	19.34	22.90	23.22	23.67	23.20	**24.20**	22.22
	75	19.17	20.17	**21.45**	18.20	21.40	20.61	21.25	19.40	21.20	21.05
	100	17.63	19.29	**20.47**	17.50	20.46	19.00	19.64	19.19	19.86	19.90
	Ave.	19.28	20.36	21.57	18.35	21.59	20.94	21.52	20.60	**21.75**	21.06
Lena	50	24.30	26.68	27.40	21.10	26.38	26.70	26.90	27.50	**27.70**	27.50
	75	21.49	24.70	25.50	20.20	24.43	24.12	24.70	25.40	25.50	**26.00**
	100	19.34	22.88	21.00	19.50	23.17	22.18	22.88	24.57	24.67	**24.80**
	Ave.	20.42	24.75	24.63	20.27	24.66	24.33	24.83	25.82	25.96	**26.10**
Barbara	50	21.30	23.25	24.30	20.11	**25.31**	24.46	23.30	22.95	22.95	24.20
	75	19.71	22.00	22.60	19.20	**23.38**	22.31	22.00	22.52	22.60	22.70
	100	18.26	20.87	21.61	18.50	**22.05**	20.80	20.87	21.70	21.78	21.88
	Ave.	19.76	22.04	22.84	19.27	**23.58**	22.52	22.06	22.39	22.44	22.93
House	50	23.36	26.20	26.60	21.00	25.76	26.30	26.70	26.27	27.23	**27.35**
	75	20.81	24.24	24.60	20.11	23.88	23.90	24.40	25.23	25.45	**25.61**
	100	18.83	22.55	22.90	19.20	22.35	21.80	22.60	23.61	**24.17**	23.60
	Ave.	19.82	24.33	24.70	20.10	24.00	24.00	24.57	25.04	**25.62**	25.52
Peppers	50	22.83	24.19	24.24	20.40	23.61	**25.26**	24.80	23.66	24.55	24.66
	75	20.46	22.38	22.27	19.40	21.50	22.65	22.55	22.88	**23.14**	22.84
	100	18.69	21.23	21.00	18.60	20.32	21.00	21.23	21.54	21.72	**21.82**
	Ave.	19.57	22.60	22.50	19.47	21.81	22.97	22.86	22.69	**23.14**	23.11
Monarch	50	22.89	24.52	25.30	20.58	24.60	25.56	25.46	25.00	**25.85**	25.19
	75	20.60	22.82	23.50	19.60	22.75	22.97	23.25	23.00	**24.00**	23.91
	100	18.85	21.50	22.20	18.70	21.50	21.13	21.65	22.30	**22.82**	22.73
	Ave.	20.78	22.95	23.67	19.63	22.95	23.22	23.45	23.43	**24.22**	23.94
Zebra	50	21.21	22.58	23.80	19.84	23.41	**24.33**	23.58	22.63	23.61	23.30
	75	19.44	20.95	22.00	18.62	21.62	21.53	21.37	21.70	**22.10**	21.66
	100	18.04	19.96	20.00	17.80	20.25	19.87	20.12	19.00	19.80	**20.55**
	Ave.	19.56	21.16	**21.93**	18.75	21.76	21.91	21.69	21.11	21.84	21.84
Average	-	19.88	22.60	23.12	19.40	22.91	22.84	23.00	23.01	**23.57**	23.50

Table 3: Comparative Image Denoising Results in terms of PSNR (dB) for High Noise Levels

($\sigma_n = 75, 100$) whereby both the shrinkage methods perform well on *Fingerprint*. This indicates that at low–medium noise levels, multilateral filtering methods in their single and multiple resolution versions can perform well on images containing fine anisotropic features at a relatively low frequency. The two variants of MRM filtering did not yield any significant gains as compared to the single-resolution multilateral filtering in the case of low–medium noise levels, with `MRM-Wav` being 0.05dB behind `MF-E` on the whole. This may be due to the fact that while decomposition of a highly noisy image into smaller resolution bands will remove a large part of the noise by virtue of smoothing and downsampling, doing so may not be greatly beneficial for images in the low–medium noise regime.

(a) 512×512 *Lena*

(b) 256×256 *House*

(c) 256×256 *Peppers*

(d) 512×512 *Barbara*

(e) 512×512 *Fingerprint*

(f) 512×512 *Monarch*

(g) 256×256 *Zebra*

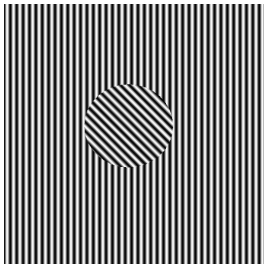

(h) 512×512 *Cosine Grating*

Figure 5: Test Images used in Our Experiments

4.2. Experiments with High Noise Levels

A comparison of denoising results on the seven test images corrupted with high levels of noise ($\sigma_n = 50, 75, 100$) for the three proposed methods with the other six methods is presented in Table 3. Since the Gaussian noise starts to exhibit similar properties to those of the salt-and-pepper noise at high levels of noise, we have also added comparative results using median filtering (`Median`), the standard method of choice at high levels of noise. It can be seen from Table 3 that at high noise levels, the proposed methods outperform all the other methods including NL-Means in almost all the cases. Although our single-resolution multilateral filtering method is 0.6dB worse on average than NL-Means at low–medium noise levels, `MRM-Wav` yields 0.75dB higher

PSNR on average than NL-Means in case of high noise levels. Note that with the exception of *Fingerprint* and *Barbara*, both the MRM variants perform consistently well for the remaining five images at all three high levels of noise. The *Fingerprint* image contains low frequency patterns of fine anisotropic features, while the *Barbara* image contains high frequency oscillatory patterns of fine anisotropic features. It is due to the presence of oscillatory patterns such as these that the two transform domain shrinkage methods, `Contourlet MD` and wave atoms respectively, perform well on these two images as they are particularly well suited to images containing periodic textures of anisotropic features. On the other hand, the MRM variants perform better than both the shrinkage methods on *Monarch* and *Zebra*, the two images containing oscillatory patterns of coarse anisotropic features for very high noise levels ($\sigma_n = 75, 100$). It is also worth noting that MRM filtering in both wavelet and Laplacian domains does not only produce better results in terms of the objective PSNR but also in terms of the subjective visual quality. Visual results for *Lena*, *Barbara*, *Peppers*, *House*, and *Monarch* images are shown in Figs. 6–10. As can be seen in these Figures, both variants of MRM filtering produce smoother ridges, sharper edges, and less *fake texture* artifacts in majority of the cases than the other methods.

5. Conclusions

In this paper, we have presented a generic framework for image denoising based on the idea of regional similarity in the spatial domain. The proposed framework is a generalization of trilateral filtering whereby multidimensional features can be used to describe local similarity. We investigated a variety of features known to capture regional properties such as textural features and edge coherence. It was shown that despite being a simple and relatively inexpensive feature to compute, local energy of a pixel in the spatial domain effectively captures the variation of intensities in its local neighborhood in the presence of additive Gaussian white noise. Analysis of the relationship between dissimilarity function used by non-local means algorithm and that based on the local energy reveals that they differ only by a weighted l_1-norm enabling local energy to be more robust in the presence of high levels of noise. It was also shown that the local energy based multilateral filtering compares favorably to other published methods in terms of both objective PSNR measure and visual quality of the denoised images.

The proposed framework was extended to multiple resolutions using wavelet

decomposition and scale space. Such an extension for bilateral filtering has been shown to remove coarse-grain noise in [35]. The wavelet variant of multiresolution multilateral (MRM) filtering was shown to produce good denoising results on images containing oscillatory patterns of anisotropic features, while the latter variant in the Laplacian domain reconstructed isotropic contents well and performed better on images containing smooth regions. Both the variants compare favorably with more sophisticated and computationally expensive shrinkage methods such as [13, 19] which are designed to capture oscillatory patterns in images. A possible future direction of this work is the development of a data-driven approach to automatically select the σ_f parameter. Another possible direction would be an extension of the proposed framework to a non-local setting, i.e., replacing the dissimilarity function in the NL-Means algorithm [21, 28] with our local energy based kernel.

Acknowledgements

Part of this work was carried out while the second author was studying for his Masters degree in Computer Science and Applications at the University of Warwick.

References

[1] P. Perona, J. Malik, Scale-space and edge detection using anisotropic diffusion, IEEE Transactions on Pattern Analysis and Machine Intelligence 12 (7) (1990) 629–639.

[2] Z. Farbman, R. Fattal, D. Lischinski, R. Szeliski, Edge-preserving decompositions for multi-scale tone and detail manipulation, Proceedings of ACM SIGGRAPH 27 (3) (2008) 67:1–67:10.

[3] O. Scherzer, J. Weickert, Relations between regularization and diffusion filtering, Journal of Mathematical Imaging and Vision 12 (1) (2000) 43–63.

[4] M. Black, G. Sapiro, D. Marimont, D. Heeger, Robust anisotropic diffusion, IEEE Transactions on Image Processing 7 (3) (1998) 421–432.

[5] D. Donoho, J. Johnstone, Ideal spatial adaptation by wavelet shrinkage, Biometrika 81 (3) (1994) 425–455.

[6] D. Donoho, X. Huo, Combined image representation using edgelets and wavelets, in: Proceedings of SPIE, Vol. 3813, 1999, pp. 468–476.

[7] C. Jung, J. Scharcanski, Adaptive image denoising and edge enhancement in scale-space using the wavelet transform, Pattern Recognition Letters 24 (7) (2003) 965–971.

[8] Z. Hou, Adaptive singular value decomposition in wavelet domain for image denoising, Pattern Recognition 36 (8) (2003) 1747–1763.

[9] E. Candes, Ridgelets: theory and applications, Ph.D. thesis, Standford University (1998).

[10] J. Starck, E. Candès, D. Donoho, The curvelet transform for image denoising, IEEE Transactions on image processing 11 (6) (2002) 670–684.

[11] M. Do, M. Vetterli, The finite ridgelet transform for image representation, IEEE Transactions on Image Processing 12 (1) (2003) 16–28.

[12] M. Do, M. Vetterli, The contourlet transform: an efficient directional multiresolution image representation, IEEE Transactions on image processing 14 (12) (2005) 2091–2106.

[13] Y. Lu, M. Do, A new contourlet transform with sharp frequency localization, in: IEEE International Conference on Image Processing, 2006, pp. 1629–1632.

[14] G. Chen, B. Kégl, Image denoising with complex ridgelets, Pattern Recognition 40 (2) (2007) 578–585.

[15] X. Wang, Wrap-around effect removal finite ridgelet transform for multiscale image denoising, Pattern Recognition 43 (11) (2010) 3693–3698.

[16] F. Meyer, R. Coifman, Brushlets: a tool for directional image analysis and image compression, Applied and computational harmonic analysis 4 (2) (1997) 147–187.

[17] Z. Yao, N. Rajpoot, Image denoising using multiscale directional cosine bases, in: Proceedings IEEE International Conference on Image Processing (ICIP), Vol. 3, 2005, pp. 313–316.

[18] M. Aharon, M. Elad, A. Bruckstein, K-SVD: An algorithm for designing overcomplete dictionaries for sparse representation, IEEE Transactions on signal processing 54 (11) (2006) 4311–4322.

[19] L. Demanet, L. Ying, Wave atoms and sparsity of oscillatory patterns, Applied and Computational Harmonic Analysis 23 (3) (2007) 368–387.

[20] N. Rajpoot, R. Wilson, Z. Yao, Planelets: A new analysis tool for planar feature extraction, in: Proceedings 5th International Workshop on Image Analysis for Multimedia Interactive Services (WIAMIS'2004), 2004.

[21] A. Buades, B. Coll, J. Morel, A non-local algorithm for image denoising, in: IEEE Conference on Computer Vision and Pattern Recognition (CVPR), Vol. 2, 2005, pp. 60–65.

[22] M. Mahmoudi, G. Sapiro, Fast image and video denoising via nonlocal means of similar neighborhoods, IEEE Signal Processing Letters 12 (12) (2005) 839–842.

[23] T. Brox, O. Kleinschmidt, D. Cremers, Efficient nonlocal means for denoising of textural patterns, IEEE Transactions on Image Processing 17 (7) (2008) 1083–1092.

[24] T. Tasdizen, Principal neighborhood dictionaries for nonlocal means image denoising, IEEE Transactions on Image Processing 18 (12) (2009) 2649–2660.

[25] D. van de Ville, M. Kocher, SURE-based non-local means, IEEE Signal Processing Letters 16 (11) (2009) 973–976.

[26] A. Foi, V. Katkovnik, K. Egiazarian, Pointwise shape-adaptive DCT for high-quality denoising and deblocking of grayscale and color images, IEEE Transactions on Image Processing 16 (5) (2007) 1395–1411.

[27] K. Dabov, A. Foi, V. Katkovnik, K. Egiazarian, Image denoising by sparse 3-d transform-domain collaborative filtering, IEEE Transactions on Image Processing 16 (8) (2007) 2080–2095.

[28] V. Katkovnik, A. Foi, K. Egiazarian, J. Astola, From local kernel to non local multiple-model image denoising, International Journal of Computer Vision 86 (1) (2009) 1–32.

[29] C. Tomasi, R. Manduchi, Bilateral filtering for gray and color images, in: International Conference on Computer Vision (ICCV), 1998, pp. 839–846.

[30] D. Barash, Fundamental relationship between bilateral filtering, adaptive smoothing, and the nonlinear diffusion equation, IEEE Transactions on Pattern Analysis and Machine Intelligence 24 (6) (2002) 844–847.

[31] R. Garnett, T. Huegerich, C. Chui, W. He, A universal noise removal algorithm with an impulse detector, IEEE Transactions on Image Processing 14 (11) (2005) 1747–1754.

[32] P. Choudhury, J. Tumblin, The trilateral filter for high contrast images and meshes, in: Proceedings of the 14th Eurographics workshop on Rendering, Eurographics Association Aire-la-Ville, Switzerland, Switzerland, 2003, pp. 186–196.

[33] Z. Yu, Z.-K. Shi, R.-Q. Wang, A multilateral filtering method applied to airplane runway image, arxiv.org (May 2008).

[34] E. Simoncelli, W. Freeman, The steerable pyramid: A flexible architecture for multi-scale derivative computation, in: Proceedings International Conference on Image Processing (ICIP), Vol. 3, 1995, pp. 444–447.

[35] M. Zhang, B. Gunturk, Multiresolution bilateral filtering for image denoising, IEEE Transactions on Image Processing 17 (12) (2008) 2324–2333.

[36] H. Yu, L. Zhao, H. Wang, Image denoising using trivariate shrinkage filter in the wavelet domain and joint bilateral filter in the spatial domain, IEEE Transactions on Image Processing 18 (10) (2009) 2364–2369.

[37] S. Chang, B. Yu, M. Vetterli, Adaptive wavelet thresholding for image denoising and compression, IEEE Transactions on Image Processing 9 (9) (2000) 1532–1546.

[38] S. Mallat, Wavelets for a vision, Proceedings of the IEEE 84 (4) (1996) 604–614.

[39] A. Bosch, A. Zisserman, X. Munoz, Representing shape with a spatial pyramid kernel, in: Proceedings of the 6th ACM international conference

on Image and video retrieval, ACM New York, NY, USA, 2007, pp. 401–408.

[40] P. Burt, E. Adelson, The Laplacian pyramid as a compact image code, IEEE Transactions on Communications 31 (4) (1983) 532–540.

[41] N. Rajpoot, Z. Yao, R. Wilson, Adaptive wavelet restoration of noisy video sequences, in: Proceedings IEEE International Conference on Image Processing (ICIP), 2004, pp. 957–960.

[42] N. Otsu, A threshold selection method from gray-level histograms, Automatica 11 (1975) 285–296.

[43] J. Xie, P. Heng, M. Shah, Image diffusion using saliency bilateral filter, IEEE Transactions on Information Technology in Biomedicine 12 (6) (2008) 768–771.

[44] L. Villemoes, Wavelet packets with uniform time-frequency localization, Comptes rendus-Mathématique 335 (10) (2002) 793–796.

(a) Noisy image; σ_n=75 (PSNR=10.66dB)

(b) Bilateral Filtering [29] (PSNR=24.70dB)

(c) `Multilateral E` (PSNR=24.70dB)

(d) Contourlet MD [13] (PSNR=25.50dB)

(e) Wave Atoms [19] (PSNR=24.43dB)

(f) NL-Means [21] (PSNR=24.12dB)

(g) `MRB` [35] (PSNR=25.40dB)

(h) `MRM-Wav` (PSNR=25.50dB)

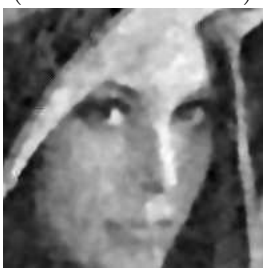

(i) `MRM-Lap` (PSNR=26.00dB)

Figure 6: Denoising Results for Central Part of the 512×512 *Lena* image; $\sigma_n = 75$.

(a) Noisy image; σ_n=75 (PSNR=10.62dB)

(b) Bilateral Filtering [29] (PSNR=22.00dB)

(c) `Multilateral E` (PSNR=22.00dB)

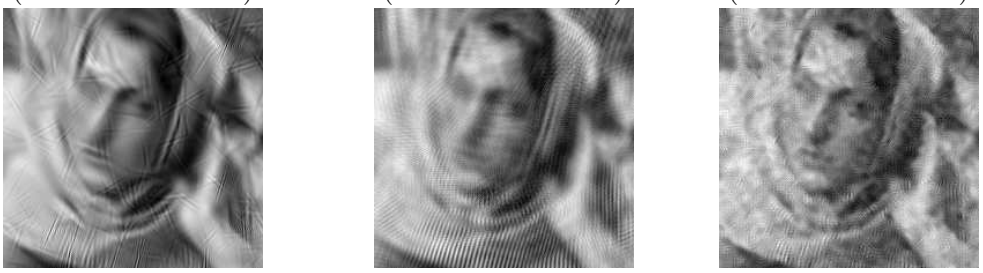

(d) Contourlet MD [13] (PSNR=22.60dB)

(e) Wave Atoms [19] (PSNR=23.38dB)

(f) NL-Means [21] (PSNR=22.31dB)

(g) `MRB` [35] (PSNR=22.52dB)

(h) `MRM-Wav` (PSNR=22.60dB)

(i) `MRM-Lap` (PSNR=22.70dB)

Figure 7: Denoising Results for Central Part of the 512×512 *Barbara* image; $\sigma_n = 75$.

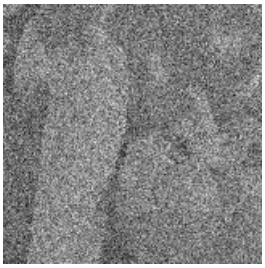

(a) Noisy image; σ_n=100 (PSNR=8.13dB)

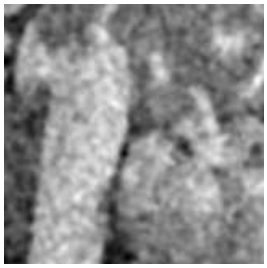

(b) Bilateral Filtering [29] (PSNR=21.23dB)

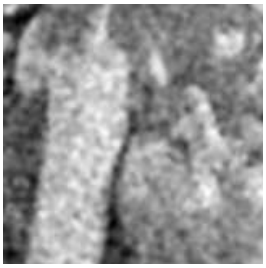

(c) `Multilateral E` (PSNR=21.23dB)

(d) Contourlet MD [13] (PSNR=21.00dB)

(e) Wave Atoms [19] (PSNR=20.32dB)

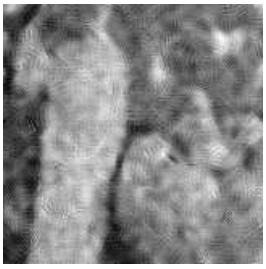

(f) NL-Means [21] (PSNR=21.00dB)

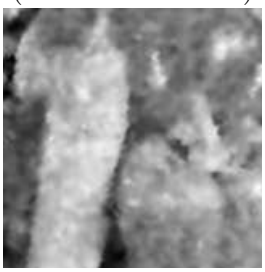

(g) `MRB` [35] (PSNR=21.54dB)

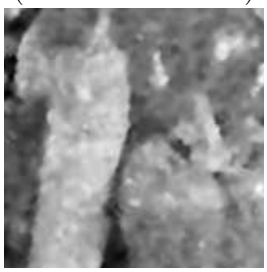

(h) `MRM-Wav` (PSNR=21.72dB)

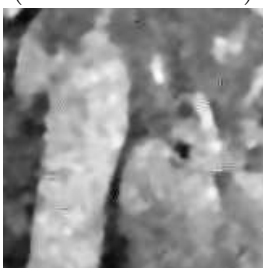

(i) `MRM-Lap` (PSNR=21.82dB)

Figure 8: Denoising Results for Central Part of the 256×256 *Peppers* image; $\sigma_n = 100$.

(a) Noisy image; σ_n=75 (PSNR=10.65dB)

(b) Bilateral Filtering [29] (PSNR=24.24dB)

(c) `Multilateral E` (PSNR=24.40dB)

(d) Contourlet MD [13] (PSNR=24.60dB)

(e) Wave Atoms [19] (PSNR=23.88dB)

(f) NL-Means [21] (PSNR=23.90dB)

(g) `MRB` [35] (PSNR=25.23dB)

(h) `MRM-Wav` (PSNR=25.45dB)

(i) `MRM-Lap` (PSNR=25.61dB)

Figure 9: Denoising Results for Central Part of the 256×256 *House* image; $\sigma_n = 75$.

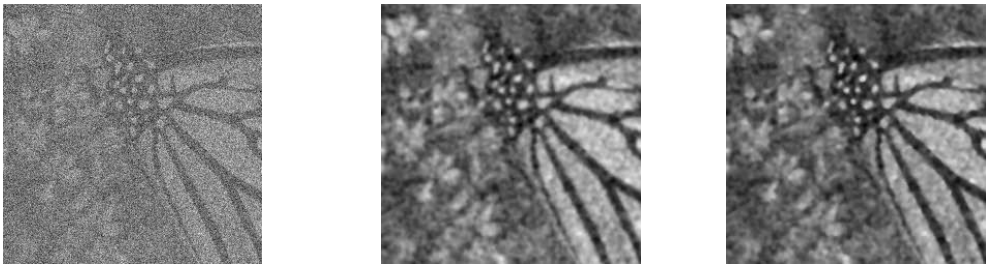

(a) Noisy image; σ_n=100 (PSNR=8.10dB)

(b) Bilateral Filtering [29] (PSNR=21.50dB)

(c) `Multilateral E` (PSNR=21.65dB)

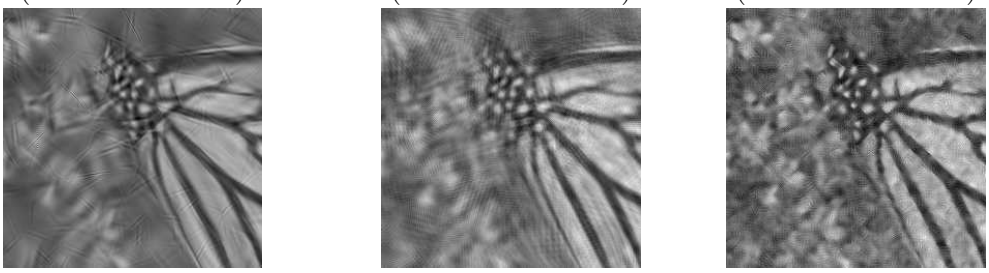

(d) Contourlet MD [13] (PSNR=22.20dB)

(e) Wave Atoms [19] (PSNR=21.50dB)

(f) NL-Means [21] (PSNR=21.13dB)

(g) MRB [35] (PSNR=22.30dB)

(h) `MRM-Wav` (PSNR=22.82dB)

(i) `MRM-Lap` (PSNR=22.73dB)

Figure 10: Denoising Results for Central Part of the 512×512 *Monarch* image; $\sigma_n = 100$.

***Author Biography**

Nasir Rajpoot received his PhD in Computer Science from the University of Warwick in 2001. Prior to that, he graduated with MSc in Systems Engineering from Quaid-e-Azam University and MSc in Computer Science from Bahauddin Zakariya University, both with the highest distinctions, in 1996 and 1994 respectively. He is currently Associate Professor in the Computer Science department at the University of Warwick. Dr Rajpoot has published more than 70 articles in peer reviewed journals and international conferences in the areas of image processing, texture analysis, and histopathology image analysis. He was the General Chair of British Machine Vision Conference (BMVC) in 2007 and the Program Chair of Medical Image Understanding and Analysis (MIUA) in 2010. A recent focus of his research has been in the areas of bioimage computing with special emphasis on pre-processing and analysis of fluorescence microscopy images with applications to cancer biology.